

Towards human SuperEEG

Lucy L. W. Owen¹, Andrew C. Heusser^{1,2}, and Jeremy R. Manning^{1*}

¹Department of Psychological and Brain Sciences, Dartmouth College,
Hanover, NH 03755, USA

²Akili Interactive,
Boston, MA 02110, USA

Abstract

Human *SuperEEG*¹ entails measuring ongoing neural activity with perfect precision and at arbitrarily high spatiotemporal resolution. Although true SuperEEG is impossible using existing methods, here we present a model-based method for *inferring* neural activity at millimeter-scale spatial resolutions and millisecond-scale temporal resolutions using standard human intracranial recordings. Our approach assumes that different people's brains exhibit similar spatial correlations, and that (all else being equal) neural activity at nearby locations will tend to be similar. One can then ask, for an arbitrary individual's brain: given recordings from a limited set of locations in that individual's brain, along with the observed spatial correlations learned from other people's recordings, how much can be inferred about ongoing activity at *other* locations in that individual's brain?

Keywords: Electrocorticography (ECoG), intracranial electroencephalography (iEEG), local field potential (LFP), epilepsy, maximum likelihood estimation, Gaussian process regression

Introduction

Modern human brain recording techniques are fraught with compromise [33]. Commonly used approaches include functional magnetic resonance imaging (fMRI), scalp electroencephalography (EEG), and magnetoencephalography (MEG). For each of these techniques, neuroscientists and electrophysiologists must choose to optimize spatial resolution at the cost of temporal resolution (e.g., as in fMRI) or temporal resolution at the cost of spatial resolution (e.g., as in EEG and MEG). A less widely used approach (due to requiring work with neurosurgical patients) is to record from electrodes implanted directly onto the cortical surface (electrocorticography; ECoG)

¹The term "SuperEEG" was coined by Robert J. Sawyer in his popular science fiction novel *The Terminal Experiment* [29]

25 or into deep brain structures (intracranial EEG; iEEG). However, these intracranial approaches
26 also require compromise: the high spatiotemporal resolutions of intracranial recordings comes
27 at the cost of substantially reduced brain coverage, since safety considerations limit the number
28 of electrodes one may implant in a given patient’s brain. Further, the locations of implanted
29 electrodes are determined by clinical, rather than research, needs.

30 An increasingly popular approach is to improve the effective spatial resolution of MEG or
31 scalp EEG data by using a geometric approach called *beamforming* to solve the biomagnetic or
32 bioelectrical inverse problem [28]. This approach entails using detailed brain conductance mod-
33 els (often informed by high spatial resolution anatomical MRI images) along with the known
34 sensor placements (localized precisely in 3D space) to reconstruct brain signals originating from
35 theoretical point sources deep in the brain (and far from the sensors). Traditional beamforming
36 approaches must overcome two obstacles. First, the inverse problem beamforming seeks to
37 solve has infinitely many solutions. Researchers have made traction towards constraining the
38 solution space by assuming that signal-generating sources are localized on a regularly spaced
39 grid spanning the brain and that individual sources are small relative to their distances to the
40 sensors [1, 11, 34]. The second, and in some ways much more serious, obstacle is that the
41 magnetic fields produced by external (noise) sources are substantially stronger than those pro-
42 duced by the neuronal changes being sought (i.e., at deep structures, as measured by sensors
43 at the scalp). This means that obtaining adequate signal quality often requires averaging the
44 measured responses over tens to hundreds of responses or trials (e.g., see review by [11]).

45 Another approach to obtaining high spatiotemporal resolution neural data has been to col-
46 lect fMRI and EEG data simultaneously. Simultaneous fMRI-EEG has the potential to balance
47 the high spatial resolution of fMRI with the high temporal resolution of scalp EEG, thereby,
48 in theory, providing the best of both worlds. In practice, however, the signal quality of both
49 recordings suffers substantially when the two techniques are applied simultaneously (e.g., see

50 review by [13]). In addition, the experimental designs that are ideally suited to each technique
51 individually are somewhat at odds. For example, fMRI experiments often lock stimulus presen-
52 tation events to the regularly spaced image acquisition time (TR), which maximizes the number
53 of post-stimulus samples. By contrast, EEG experiments typically employ jittered stimulus pre-
54 sentation times to maximize the experimentalist’s ability to distinguish electrical brain activity
55 from external noise sources such as from 60 Hz alternating current power sources.

56 The current “gold standard” for precisely localizing signals and sampling at high temporal
57 resolution is to take (ECoG or iEEG) recordings from implanted electrodes (but from a limited
58 set of locations in any given brain). This begs the following question: what can we infer
59 about the activity exhibited by the rest of a person’s brain, given what we learn from the
60 limited intracranial recordings we have from their brain and additional recordings taken from
61 *other* people’s brains? Here we develop an approach, which we call *SuperEEG*, based on
62 Gaussian process regression [27]. SuperEEG entails using data from multiple people to estimate
63 activity patterns at arbitrary locations in each person’s brain (i.e., independent of their electrode
64 placements). We test SuperEEG approach using two large datasets of intracranial recordings [7,
65 8, 12, 16–19, 21, 23, 30–32, 35, 40]. We show that the SuperEEG algorithm recovers signals well
66 from electrodes that were held out of the training dataset. We also examine the factors that
67 influence how accurately activity may be estimated (recovered), which may have important
68 implications for electrode design and placement in neurosurgical applications.

69 Approach

70 The SuperEEG approach to inferring high temporal resolution full-brain activity patterns is
71 outlined and summarized in Figure 1. We describe (in this section) and evaluate (in *Results*) our
72 approach using a two large previously collected dataset comprising multi-session intracranial
73 recordings. Dataset 1 comprises multi-session recordings taken from 6876 electrodes implanted

74 in the brains of 88 epilepsy patients [21, 23, 30–32]. Each recording session lasted from 0.3–
75 14.2 hours (Fig. S4A), and includes data recorded roughly from when the patients woke up
76 each morning, to before they went to sleep at the end of each day. In addition to typical
77 bed-ridden hospital patient activities (e.g., lying in bed, reading, watching television, using
78 personal electronic devices, listening to music, visiting with family and friends, etc.), the pa-
79 tients also performed a variety of experimental cognitive tasks throughout their day (primarily
80 list-learning memory tasks). For the purposes of the Dataset 1 analyses presented here, we
81 aggregated all data across each recording session, ignoring the particular activities or tasks
82 the patients were performing at any given moment. We used Dataset 1 to develop our main
83 SuperEEG approach, and to examine the extent to which SuperEEG might be able to generate
84 task-general predictions. Dataset 2 comprised multi-session recordings from 3159 electrodes
85 implanted in the brains of 24 epilepsy patients [7, 8, 12, 16–19, 35, 40]. Each recording session
86 lasted from .4–6.6 hours (Fig. S4B). Whereas Dataset 1 included recordings taken during a wide
87 variety of behaviors, Dataset 2 included recordings taken as each patient performed each of
88 two memory tasks: a random word list free recall task and a categorized word list free recall
89 task. We used Dataset 2 to further examine the ability of SuperEEG to generalize its predictions
90 within versus across tasks. Figure S4 provides additional details on both datasets.

91 We first applied fourth order Butterworth notch filter to remove 60 Hz ($\pm .5$ Hz) line noise
92 from every recording (from every electrode). Next, we downsampled the recordings (regardless
93 of the original samplerate) to 250 Hz. (This downsampling step served to both normalize for
94 differences in sampling rates across patients and to ease the computational burden of our sub-
95 sequent analyses.) We then excluded any electrodes that showed putative epileptiform activity.
96 Specifically, we excluded from further analysis any electrode that exhibited an average kurtosis
97 of 10 or greater across all of that patient’s recording sessions. We also excluded any patients
98 with fewer than 2 electrodes that passed this criteria, as the SuperEEG algorithm requires

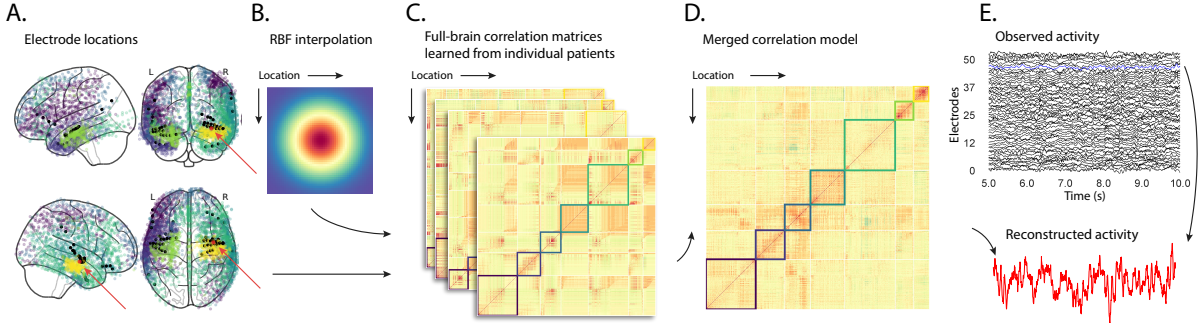


Figure 1: Methods overview. **A. Electrode locations.** Each dot reflects the location of a single electrode implanted in the brain of a Dataset 1 patient. A held-out recording location from one patient is indicated in red, and the patient’s remaining electrodes are indicated in black. The electrodes from the remaining patients are colored by k -means cluster (computed using the full-brain correlation model shown in Panel D). **B. Radial basis function kernel.** Each electrode contributed by the patient (black) weights on the full set of locations under consideration (all dots in Panel A, defined as \bar{R} in the text). The weights fall off with positional distance (in MNI space) according to an RBF. **C. Per-patient correlation matrices.** After computing the pairwise correlations between the recordings from each patient’s electrodes, we use RBF-weighted averages to estimate correlations between all locations in \bar{R} . We obtain an estimated full-brain correlation matrix using each patient’s data. **D. Merged correlation model.** We combine the per-patient correlation matrices (Panel C) to obtain a single full-brain correlation model that captures information contributed by every patient. Here we have sorted the rows and columns to reflect k -means clustering labels [using $k=7$; 41], whereby we grouped locations based on their correlations with the rest of the brain (i.e., rows of the matrix displayed in the panel). The boundaries denote the cluster groups. The rows and columns of Panel C have been sorted using the Panel D-derived cluster labels. **E. Reconstructing activity throughout the brain.** Given the observed recordings from the given patient (shown in black; held-out recording is shown in blue), along with a full-brain correlation model (Panel D), we use Equation 12 to reconstruct the most probable activity at the held-out location (red).

99 measuring correlations between 2 or more electrodes from each patient. For Dataset 1, this
100 yielded clean recordings from 4168 electrodes implanted throughout the brains of 67 patients
101 (Fig. 1A); for Dataset 2, this yielded clean recordings from 3159 electrodes from 24 patients.
102 Each individual patient contributes electrodes from a limited set of brain locations, which we
103 localized in a common space [MNI152; 10]; an example Dataset 1 patient's 54 electrodes that
104 passed the predefined kurtosis test are highlighted in black and red.

The recording from a given electrode is maximally informative about the activity of the neural tissue immediately surrounding its recording surface. However, brain regions that are distant from the recording surface of the electrode also contribute to the recording, albeit (*ceteris paribus*) to a much lesser extent. One mechanism underlying these contributions is volume conduction. The precise rate of falloff due to volume conduction (i.e., how much a small volume of brain tissue at location x contributes to the recording from an electrode at location η) depends on the size of the recording surface, the electrode's impedance, and the conductance profile of the volume of brain between x and η . As an approximation of this intuition, we place a Gaussian radial basis function (RBF) at the location η of each electrode's recording surface (Fig. 1B). We use the values of the RBF at any brain location x as a rough estimate of how much structures around x contributed to the recording from location η :

$$\text{rbf}(x|\eta, \lambda) = \exp \left\{ -\frac{\|x - \eta\|^2}{\lambda} \right\}, \quad (1)$$

105 where the width variable λ is a parameter of the algorithm (which may in principle be set
106 according to location-specific tissue conductance profiles) that governs the level of spatial
107 smoothing. In choosing λ for the analyses presented here, we sought to maximize spatial
108 resolution (which implies a small value of λ) while also maximizing the algorithm's ability
109 to generalize to any location throughout the brain, including those without dense electrode
110 coverage (which implies a large value of λ). Here we set $\lambda = 20$, guided in part by our prior
111 work [22, 24], and in part by examining the brain coverage with non-zero weights achieved by

112 placing RBFs at each electrode location in Dataset 1 and taking the sum (across all electrodes)
 113 at each voxel in a 4 mm³ MNI brain. (We then held λ fixed for our analyses of Dataset 2.) We
 114 note that this value could in theory be further optimized, e.g., using cross validation or a formal
 115 model [e.g., 24].

116 A second mechanism whereby a given region x can contribute to the recording at η is
 117 through (direct or indirect) anatomical connections between structures near x and η . We use
 118 temporal correlations in the data to estimate these anatomical connections [2]. Let \bar{R} be the
 119 set of locations at which we wish to estimate local field potentials, and let $R_s \subseteq \bar{R}$ be set of
 120 locations at which we observe local field potentials from patient s (excluding the electrodes that
 121 did not pass the kurtosis test described above). In the analyses below we define $\bar{R} = \cup_{s=1}^S R_s$.
 122 We can calculate the expected inter-electrode correlation matrix for patient s , where $C_{s,k}(i, j)$ is
 123 the correlation between the time series of voltages for electrodes i and j from subject s during
 124 session k , using:

$$\bar{C}_s = r\left(\frac{1}{n}\left(\sum_{k=1}^n z(C_{s,k})\right)\right), \text{ where} \quad (2)$$

$$z(r) = \frac{\log(1+r) - \log(1-r)}{2} \text{ is the Fisher } z\text{-transformation and} \quad (3)$$

$$z^{-1}(z) = r(z) = \frac{\exp(2z) - 1}{\exp(2z) + 1} \text{ is its inverse.} \quad (4)$$

125 Next, we use Equation 1 to construct a number of to-be-estimated locations by number of
 126 patient electrode locations weight matrix, W_s . Specifically, W_s approximates how informative
 127 the recordings at each location in R_s are in reconstructing activity at each location in \bar{R} , where
 128 the contributions fall off with an RBF according to the distances between the corresponding
 129 locations:

$$W_s(i, j) = \text{rbf}(i|j, \lambda). \quad (5)$$

Given this weight matrix, W_s , and the observed inter-electrode correlation matrix for patient s , \bar{C}_s , we can estimate the correlation matrix for all locations in \bar{R} (\hat{C}_s ; Fig. 1C) using:

$$\hat{N}_s(x, y) = \sum_{i=1}^{|R_s|} \sum_{j=1}^{i-1} W(x, i) \cdot W(y, j) \cdot z(\bar{C}_s(i, j)) \quad (6)$$

$$\hat{D}_s(x, y) = \sum_{i=1}^{|R_s|} \sum_{j=1}^{i-1} W(x, i) \cdot W(y, j). \quad (7)$$

$$\hat{C}_s = r\left(\frac{\hat{N}_s}{\hat{D}_s}\right). \quad (8)$$

After estimating the numerator (\hat{N}_s) and denominator (\hat{D}_s) placeholders for each \hat{C}_s , we aggregate these estimates across the S patients to obtain a single expected full-brain correlation matrix (\hat{K} ; Fig. 1D):

$$\hat{K} = r\left(\frac{\sum_{s=1}^S \hat{N}_s}{\sum_{s=1}^S \hat{D}_s}\right). \quad (9)$$

Intuitively, the numerators capture the general structures of the patient-specific estimates of full-brain correlations, and the denominators account for which locations were near the implanted electrodes in each patient. To obtain \hat{K} , we compute a weighted average across the estimated patient-specific full-brain correlation matrices, where patients with observed electrodes near a particular set of locations in \hat{K} contribute more to the estimate.

Having used the multi-patient data to estimate a full-brain correlation matrix at the set of locations in \bar{R} that we wish to know about, we next use \hat{K} to estimate activity patterns everywhere in \bar{R} , given observations at only a subset of locations in \bar{R} (Fig. 1E).

Let α_s be the set of indices of patient s 's electrode locations in \bar{R} (i.e., the locations in R_s), and let β_s be the set of indices of all other locations in \bar{R} . In other words, β_s reflects the locations

¹⁴² in \bar{R} where we did not observe a recording for patient s (these are the recording locations we
¹⁴³ will want to fill in using SuperEEG). We can sub-divide \hat{K} as follows:

$$\hat{K}_{\beta_s, \alpha_s} = \hat{K}(\beta_s, \alpha_s), \text{ and} \quad (10)$$

$$\hat{K}_{\alpha_s, \alpha_s} = \hat{K}(\alpha_s, \alpha_s). \quad (11)$$

¹⁴⁴ Here $\hat{K}_{\beta_s, \alpha_s}$ represents the correlations between the “unknown” activity at the locations in β_s
¹⁴⁵ and the observed activity at the locations in α_s , and $\hat{K}_{\alpha_s, \alpha_s}$ represents the correlations between
¹⁴⁶ the observed recordings (at the locations in α_s).

¹⁴⁷ Let Y_{s,k,α_s} be the number-of-timepoints (T) by $|\alpha_s|$ matrix of (observed) voltages from the
¹⁴⁸ electrodes in α_s during session k from patient s . Then we can estimate the voltage from patient
¹⁴⁹ s ’s k^{th} session at the locations in β_s using [27]:

$$\hat{Y}_{s,k,\beta_s} = ((\hat{K}_{\beta_s, \alpha_s} \cdot \hat{K}_{\alpha_s, \alpha_s}^{-1}) \cdot Y_{s,k,\alpha_s}^T)^T. \quad (12)$$

¹⁵⁰ This equation is the foundation of the SuperEEG algorithm. Whereas we observe recordings
¹⁵¹ only at the locations indexed by α_s , Equation 12 allows us to estimate the recordings at all loca-
¹⁵² tions indexed by β_s , which we can define *a priori* to include any locations we wish, throughout
¹⁵³ the brain. This yields estimates of the time-varying voltages at *every* location in \bar{R} , provided that
¹⁵⁴ we define \bar{R} in advance to include the union of all of the locations in R_s and all of the locations
¹⁵⁵ at which we wish to estimate recordings (i.e., a timeseries of voltages).

¹⁵⁶ We designed our approach to be agnostic to electrode impedances, as electrodes that do not
¹⁵⁷ exist do not have impedances. Therefore our algorithm recovers voltages in standard deviation
¹⁵⁸ (z -scored) units rather than attempting to recover absolute voltages. (This property reflects
¹⁵⁹ the fact that $\hat{K}_{\beta_s, \alpha_s}$ and $\hat{K}_{\alpha_s, \alpha_s}$ are correlation matrices rather than covariance matrices.) Also,
¹⁶⁰ note that Equation 12 requires computing a T by T matrix, which can become computationally

¹⁶¹ intractable when T is very large (e.g., for the patient highlighted in Fig. 2, $T = 12786750$).
¹⁶² However, because Equation 12 is time invariant, we may compute Y_{s,k,β_s} in a piecewise manner
¹⁶³ by filling in Y_{s,k,β_s} one row at a time (using the corresponding samples from Y_{s,k,α_s}).

¹⁶⁴ The SuperEEG algorithm described above and in Figure 1 allows us to estimate, up to a
¹⁶⁵ constant scaling factor, local field potentials (LFPs) for each patient at all arbitrarily chosen
¹⁶⁶ locations in the set \bar{R} , even if we did not record that patient's brain at all of those locations. We next
¹⁶⁷ turn to an evaluation of the accuracy of those estimates.

¹⁶⁸ Results

¹⁶⁹ We used a cross-validation approach to test the accuracy with which the SuperEEG algorithm
¹⁷⁰ reconstructs activity throughout the brain. For each patient in turn, we estimated full-brain
¹⁷¹ correlation matrices (Eqn. 9) using data from all of the *other* patients. This step ensured that the
¹⁷² data we were reconstructing could not also be used to estimate the between-location correlations
¹⁷³ that drove the reconstructions via Equation 12 (otherwise the analysis would be circular). For
¹⁷⁴ that held-out patient, for each of their electrodes in turn, we used Equation 12 to reconstruct
¹⁷⁵ activity at the held-out electrode location, using the correlation matrix learned from all other
¹⁷⁶ patients' data as \hat{K} , and using activity recorded from the other electrodes from the held-out
¹⁷⁷ patient as Y_{s,k,α_s} . We then asked: how closely did each of the SuperEEG-estimated recordings
¹⁷⁸ at those electrodes match the observed recordings from those electrodes (i.e., how closely did
¹⁷⁹ the estimated \hat{Y}_{s,k,β_s} match the observed Y_{s,k,β_s} ?).

¹⁸⁰ To illustrate our approach, we first examine an individual held-out raw LFP trace and its
¹⁸¹ associated SuperEEG-derived reconstruction. Figure 2A displays the observed LFP from the red
¹⁸² electrode in Figure 1A (blue), and its associated reconstruction (red), during a 5 s time window
¹⁸³ during one of the example patient's six recording sessions. The two traces match closely
¹⁸⁴ ($r = 0.869, p < 10^{-10}$). Figure 2B displays a two-dimensional histogram of the actual versus

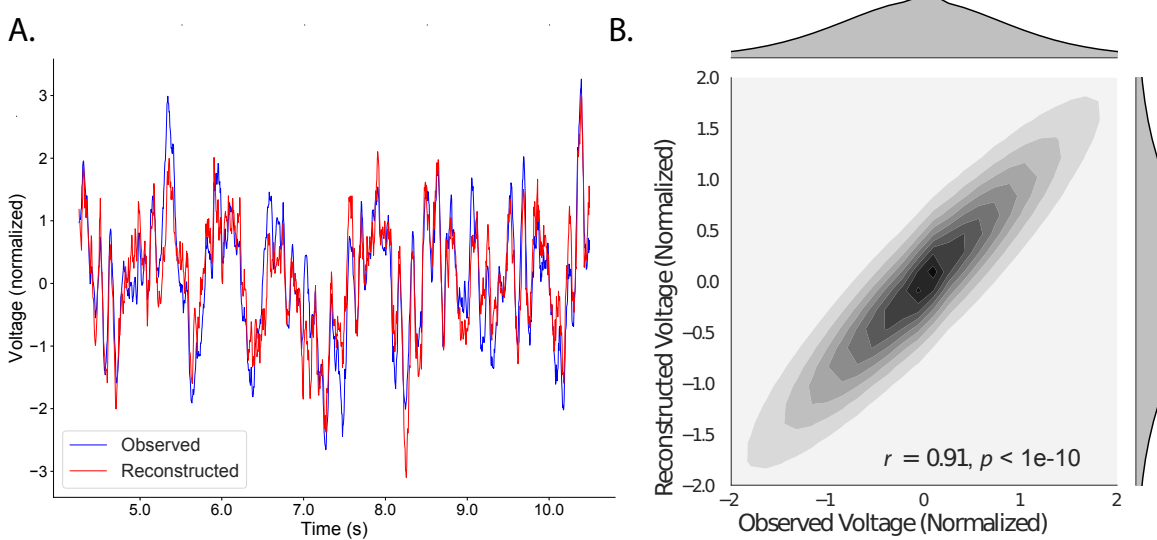


Figure 2: Observed and reconstructed LFP from a single electrode. **A. Example LFP.** A 5 s recording from the red electrode in Figure 1A is displayed in blue, and the reconstructed LFP during the same time window is shown in red. **B. Observed versus reconstructed LFP over 14.2 hours.** The two-dimensional histogram reflects the relation between distributions of observed versus reconstructed voltages from one patient, across the 14.2 hours of recorded data collected over 6 recording sessions. The correlation reported in the panel is between the observed and reconstructed voltages. Both panels: all voltages are represented in standard deviation units (computed within session).

reconstructed voltages for the entire 14.2 total hours of recordings from the example electrode (correlation: $r = 0.909, p < 10^{-10}$). This example confirms that the SuperEEG algorithm recovers the recordings from this single electrode well. Next, we used this general approach to quantify the algorithm's performance across the full dataset.

For each held-out electrode, from each held-out patient in turn, we computed the average correlation (across recording sessions) between the SuperEEG-reconstructed voltage traces and the observed voltage traces from that electrode. For this analysis we set \bar{R} to be the union of all electrode locations across all patients. This yielded a single correlation coefficient for each electrode location in \bar{R} , reflecting how well the SuperEEG algorithm was able to recover the recording at that location by incorporating data across patients (black histogram in Fig. 3A, map

195 in Fig. 3C). The observed distribution of correlations was centered well above zero (mean: 0.52;
196 t -test comparing mean of distribution of z -transformed per-electrode correlation coefficients to
197 0: $t(66) = 25.08, p < 10^{-30}$), indicating that the SuperEEG algorithm recovers held-out activity
198 patterns substantially better than random guessing.

199 As a stricter benchmark, we compared the quality of these across-participant reconstructions
200 (i.e., computed using a correlation model learned from other patients' data) to reconstructions
201 generated using a correlation model trained using the in-patient's data. In other words, for
202 this within-patient benchmark analysis we estimated \hat{C}_s (Eqn. 8) for each patient in turn, using
203 recordings from all of that patient's electrodes except at the location we were reconstructing.
204 These within-patient reconstructions serve as an estimate of how well data from all of the other
205 electrodes from that single patient may be used to estimate held-out data from the same patient.
206 This allows us to ask how much information about the activity at a given electrode might be
207 inferred through (a) volume conductance or other sources of "leakage" from activity patterns
208 measured from the patient's other electrodes and (b) across-electrode correlations learned from
209 that single patient. As shown in Figure 3A (gray histogram), the distribution of within-patient
210 correlations was centered well above zero (mean: 0.32; t -test comparing mean of distribution of
211 z -transformed per-electrode correlation coefficients to 0: $t(66) = 15.16, p < 10^{-20}$). However, the
212 across-patient correlations were substantially higher (t -test comparing average z -transformed
213 within versus across patient electrode correlations: $t(66) = 9.62, p < 10^{-10}$). This is an especially
214 conservative test, given that the across-patient SuperEEG reconstructions exclude (from the
215 correlation matrix estimates) all data from the patient whose data is being reconstructed. We
216 repeated each of these analyses on a second independent dataset and found similar results
217 (Fig. 3B, D; within versus across reconstruction accuracy: $t(23) = 6.93, p < 10^{-5}$). We also
218 replicated this result separately for each of the two experiments from Dataset 2 (Fig. S1). This
219 overall finding, that reconstructions of held-out data using correlation models learned from

220 *other* patient's data yield higher reconstruction accuracy than correlation models learned from
221 the patient whose data is being reconstructed, has two important implications. First, it implies
222 that distant electrodes provide additional predictive power to the data reconstructions beyond
223 the information contained solely in nearby electrodes. (This follows from the fact that each
224 patient's electrodes are implanted in a unique set of locations, so for any given electrode the
225 closest electrodes in the full dataset are likely to come from the same patient.) Second, it implies
226 that the spatial correlations learned using the SuperEEG algorithm are, to some extent, similar
227 across people.

228 The recordings we analyzed from Dataset 1 comprised data collected as the patients per-
229 formed a variety of (largely idiosyncratic) tasks throughout each day's recording session. That
230 we observed reliable reconstruction accuracy across patients suggests that the spatial correla-
231 tions derived from the SuperEEG algorithm are, to some extent, similar across tasks. We tested
232 this finding more explicitly using Dataset 2. In Dataset 2, the recordings were limited to times
233 when each patient was participating in each of two experiments (Experiment 1, a random-word
234 list free recall task, and Experiment 2, a categorized list free recall task). We wondered whether
235 a correlation model learned from data from one experiment might yield good predictions of
236 data from the other experiment. Further, we wondered about the extent to which it might be
237 beneficial or harmful to combine data across tasks.

238 To test the task-specificity of the SuperEEG-derived correlation models, we repeated the
239 above within- and across-patient cross validation procedures separately for Experiment 1 and
240 Experiment 2 data from Dataset 2. We then compared the reconstruction accuracies for held-out
241 electrodes, for models trained within versus across the two experiments, or combining across
242 both experiments (Fig. S2). In every case we found that across-patient models trained using
243 data from all other patients out-performed within-patient models trained on data only from the
244 subject contributing the given electrode ($ts(24) > 6.50, ps < 10^{-5}$). All reconstruction accuracies

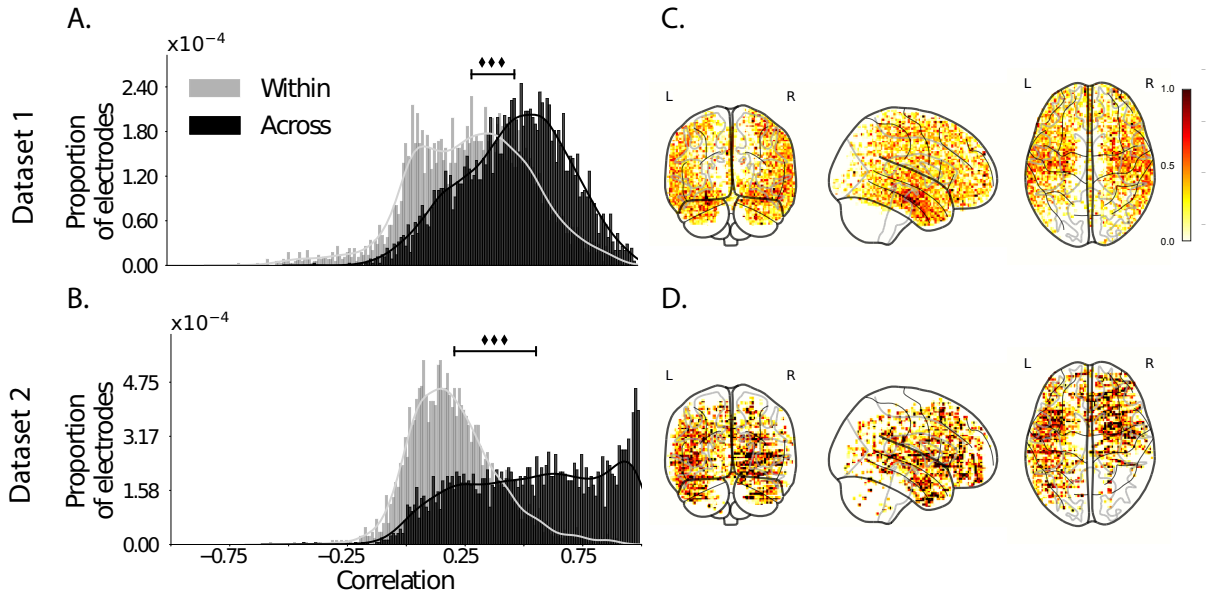


Figure 3: Reconstruction quality across all electrodes in two ECoG datasets. A. Distributions of correlations between observed versus reconstructed activity by electrode, for Dataset 1. The across-patient distribution (black) reflects reconstruction accuracy (correlation) using a correlation model learned from all but one patient’s data, and then applied to that held-out patient’s data. The within-patient distribution (gray) reflects performance using a correlation model learned from the same patient who contributed the to-be-reconstructed electrode. **B. Distributions of correlations for Dataset 2.** This panel is in the same format as Panel A, but reflects results obtained from Dataset 2. The histograms aggregate data across both Dataset 2 experiments; for results broken down by experiment see Figure S3. **C.–D. Reconstruction performance by location.** Each dot reflects the location of a single implanted electrode from Dataset 1 (Panel C) or Dataset 2 (Panel D). The dot colors denote the average across-session correlation, using the across-patient correlation model, between the observed and reconstructed activity at the given electrode location.

245 also reliably exceeded chance performance ($t_{s(24)} > 8.00$, $p < 10^{-8}$). Average reconstruction
246 accuracy was highest for the across-patient models limited to data from the same experiment
247 (mean accuracy: 0.68); next-highest for the across-patient models that combined data across
248 both experiments (mean accuracy: 0.61); and lowest for models trained across task (mean
249 accuracy: 0.47). This result also held for each of the Dataset 2 experiments individually
250 (Fig. S3). Taken together, these results indicate that there are reliable commonalities in the spatial
251 correlations of full-brain activity across tasks, but that there are also reliable differences in these
252 spatial correlations across tasks. Whereas reconstruction accuracy benefits from incorporating
253 data from other patients, reconstruction accuracy is highest when constrained to within-task
254 data, or data that includes a variety of tasks (e.g., Dataset 1, or combining across the two Dataset
255 2 experiments).

256 Although both datasets we examined provide good full-brain coverage (when considering
257 data from every patient; e.g. Fig. 3C, D), electrodes are not placed uniformly throughout the
258 brain. For example, electrodes are more likely to be implanted in regions like the medial
259 temporal lobe (MTL), and are rarely implanted in occipital cortex (Fig. 4A, B). Separately for
260 each dataset, for each voxel in the 4 mm^3 voxel MNI152 brain, we computed the proportion
261 of electrodes in the dataset that were contained within a 20 MNI unit radius sphere centered
262 on that voxel. We defined the *density* at that location as this proportion. Across Datasets
263 1 and 2, the electrode placement densities were similar (correlation by voxel: $r = 0.56$, $p <$
264 10^{-10}). We wondered whether regions with good coverrage might be associated with better
265 reconstruction accuracy (e.g. Fig. 3C, D indicate that many electrodes in the MTL have relatively
266 high reconstruction accuracy, and occipital electrodes tend to have relatively low reconstruction
267 accuracy). To test whether this held more generally across the entire brain, for each dataset
268 we computed the electrode placement density for each electrode from each patient (using
269 the proportion of *other* patients' electrodes within 20 MNI units of the given electrode). We

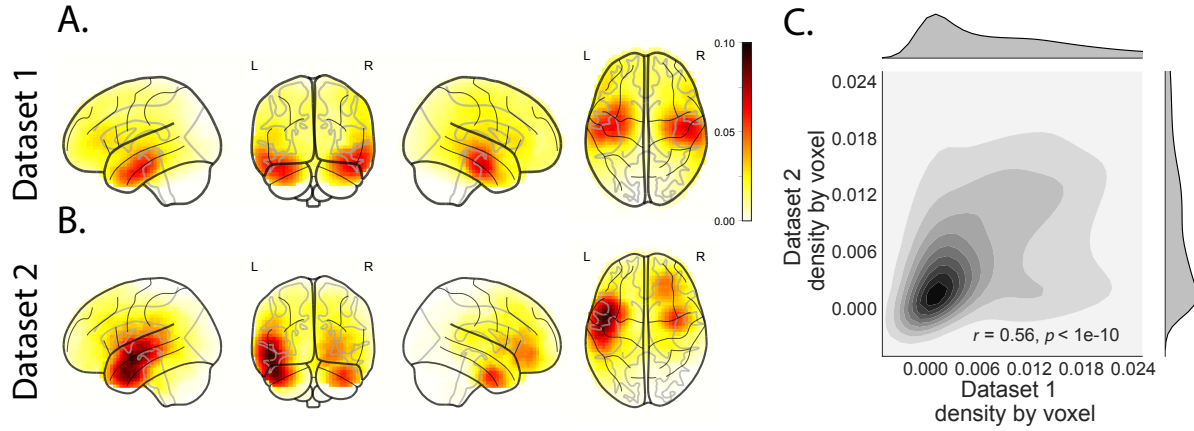


Figure 4: Electrode sampling density by location. **A. Electrode sampling density by voxel in Dataset 1.** Each voxel is colored by the proportion of total electrodes in the dataset that are located within a 20 MNI unit radius sphere centered on the given voxel. **B. Electrode sampling density by voxel in Dataset 2.** This panel displays the sampling density map for Dataset 2, in the same format as Panel A. **C. Correspondence in sampling density by voxel across Datasets 1 and 2.** The two-dimensional histogram displays the by-voxel densities in the two Datasets, and the one-dimensional histograms display the proportions of voxels in each dataset with the given density value. The correlation reported in the panel is across voxels in the 4 mm^3 MNI brain.

then correlated these density values with the across-patient reconstruction accuracies for each electrode. Contrary to our expectation, rather than positive correlations, we found weak (but reliable) negative correlations between reconstruction accuracy and density for both datasets (Dataset 1: $r = -0.07, p < 10^{-5}$; Dataset 2: $r = -0.18, p < 10^{-10}$). This indicates that the reconstruction accuracies we observed are not driven solely by sampling density, but rather may also reflect higher order properties of neural dynamics such as functional correlations between distant voxels [3].

In neurosurgical applications where one wishes to infer full-brain activity patterns, can our framework yield insights into where the electrodes should be placed? A basic assumption of our approach (and of most prior ECoG work) is that electrode recordings are most informative about the neural activity near the recording surface of the electrode. But if we consider that activity patterns throughout the brain are meaningfully correlated, are there particular implantation

locations that, if present in a patient’s brain, yield especially high reconstruction accuracies throughout the rest of the brain? For example, one might hypothesize that brain structures that are heavily interconnected with many other structures could be more informative about full-brain activity patterns than comparatively isolated structures.

To gain insights into whether particular electrode locations might be especially informative, we first computed the average reconstruction accuracy across all of each patient’s electrodes (using the across-patients cross validation test; black histograms in Fig. 3A and B). We labeled each patient’s electrodes in each dataset with the average reconstruction accuracy for that patient. In other words, we assigned every electrode from each given patient the same value, reflecting how well the activity patterns at those electrodes were reconstructed on average. Next, for each voxel in the 4 mm³ MNI brain, we computed the average value across any electrode (from any patient) that came within 20 MNI units of that voxel’s center. Effectively, we computed an *information score* for each voxel, reflecting the average reconstruction accuracy across any patients with electrodes near each voxel—where the averages were weighted to reflect patients who had more electrodes implanted near that location. This yielded a single map for each dataset, highlighting regions that are potentially promising implantation targets in terms of providing full-brain activity information via SuperEEG (Fig. 5A, B). Despite task and patient differences across the two datasets, we nonetheless found that the maps of the most promising implantation targets derived from both datasets were similar (voxelwise correlation between information scores across the two datasets: $r = 0.23, p < 10^{-10}$). While the correspondence between the two maps was not perfect, our finding that there were some commonalities between the two maps lends support to the notion that different brain areas are differently informative about full-brain activity patterns. Further, regions like the right post central gyrus, right supramarginal gyrus, and the right nucleus accumbens that exhibited strong information scores in both datasets may be especially promising implantation targets.

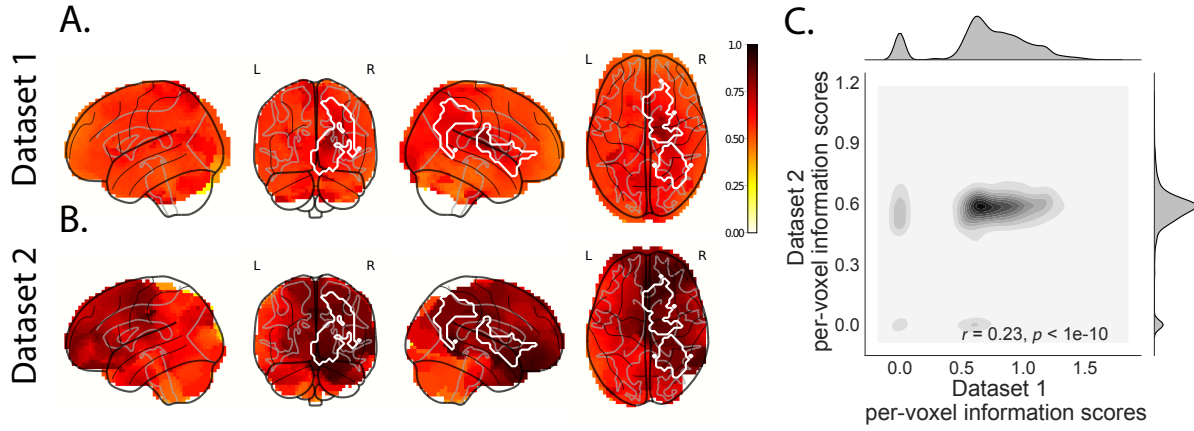


Figure 5: Most informative electrode locations. **A. Dataset 1 information score by voxel.** The voxel colors reflect the weighted average reconstruction accuracy across all electrodes from any patients with at least one electrode within 20 MNI units of the given voxel. **B. Dataset 2 information score by voxel.** This panel is in the same format as Panel A. In Panels A and B the contours indicate the intersections between the top 10% most informative voxels in each map. **C. Correspondence in information scores by voxel across Datasets 1 and 2.** Same format as Figure 4C.

307 Discussion

308 Are our brain's networks static or dynamic? And to what extent are the network properties
 309 of our brains stable across people and tasks? One body of work suggests that our brain's
 310 *functional* networks are dynamic [e.g., 24], person-specific [e.g., 9], and task-specific [e.g.,
 311 39]. In contrast, although the gross anatomical structure of our brains changes meaningfully
 312 over the course of years as our brains develop, on the timescales of typical neuroimaging ex-
 313 periments (i.e., hours to days) our anatomical networks are largely stable [e.g., 4]. Further,
 314 many aspects of brain anatomy, including white matter structure, are largely preserved across
 315 people [e.g., 15, 26, 37]. There are several possible means of reconciling this apparent inconsis-
 316 tency between dynamic person- and task-specific functional networks versus stable anatomical
 317 networks. For example, relatively small magnitude anatomical differences across people may
 318 be reflected in reliable functional connectivity differences. Along these lines, one recent study

319 found that diffusion tensor imaging (DTI) structural data is similar across people, but may be
320 used to predict person-specific resting state functional connectivity data [2]. Similarly, other
321 work indicates that task-specific functional connectivity may be predicted by resting state func-
322 tional connectivity data [5, 38]. Another (potentially complementary) possibility is that our
323 functional networks are constrained by anatomy, but nevertheless exhibit (potentially rapid)
324 task-dependent changes [e.g., 36].

325 Here we have taken a model-based approach to studying whether high spatiotemporal
326 resolution activity patterns throughout the human brain may be explained by a static connec-
327 tome model that is shared across people and tasks. Specifically, we trained a model to take
328 in recordings from a subset of brain locations, and then predicted activity patterns during the
329 same interval, but at *other* locations that were held out from the model. Our model, based on
330 Gaussian process regression, was built on three general hypotheses about the nature of the
331 correlational structure of neural activity (each of which we tested). First, we hypothesized that
332 functional correlations are stable over time and across tasks. We found that, although aspects
333 of the patients' functional correlations that were stable across tasks, we achieved better recon-
334 struction accuracy when we trained the model on within-task data [we acknowledge that our
335 general approach could potentially be extended to better model across-task changes, following
336 5, 38, and others]. Second, we hypothesized that some of the correlational structure of peo-
337 ple's brain activity is similar across individuals. Consistent with this hypothesis, our model
338 explained the data best when we trained the correlation model using data from *other* patients—
339 even when compared to a correlation model trained on the same patient's data. Third, we
340 resolved ambiguities in the data by hypothesizing that neural activity from nearby sources will
341 tend to be similar, all else being equal. This hypothesis was supported through our finding that
342 all of the models we trained that incorporated this spatial smoothness assumption predicted
343 held-out data well above chance.

344 One potential limitation of our approach is that it does not provide a natural means of
345 estimating the precise timing of single-neuron action potentials. Prior work has shown that
346 gamma band and broadband activity in the LFP may be used to estimate the firing rates of
347 neurons that underly the population contributing to the LFP [6, 14, 20, 25]. Because SuperEEG
348 reconstructs LFPs throughout the brain, one could in principle use gamma or broadband power
349 in the reconstructed signals to estimate the corresponding firing rates (though not the timings
350 of individual action potentials).

351 Beyond providing a means of estimating ongoing activity throughout the brain using al-
352 ready implanted electrodes, our work also has implications for where to place the electrodes in
353 the first place. Electrodes are typically implanted to maximize coverage of suspected epilep-
354 togenic tissue. However, our findings suggest that this approach could be further optimized.
355 Specifically, one could leverage not only the non-invasive recordings taken during an initial
356 monitoring period (as is currently done routinely), but also recordings collected from other
357 patients. We could then ask: given what we learn from other patients' data (and potentially
358 from the scalp EEG recordings of this new patient), where should we place a fixed number of
359 electrodes to maximize our ability to map seizure foci? As shown in Figure 5, recordings from
360 different locations are differently informative in terms of reconstructing the spatiotemporal
361 activity patterns throughout the brain. This property might be leveraged in decisions about
362 where to surgically implant electrodes in future patients.

363 **Concluding remarks**

364 Over the past several decades, neuroscientists have begun to leverage the strikingly profound
365 mathematical structure underlying the brain's complexity to infer how our brains carry out
366 computations to support our thoughts, actions, and physiological processes. Whereas tradi-
367 tional beamforming techniques rely on geometric source-localization of signals measured at the

368 scalp, here we propose an alternative approach that leverages the rich correlational structure
369 of two large datasets of human intracranial recordings. In doing so, we are one step closer to
370 observing, and perhaps someday understanding, the full spatiotemporal structure of human
371 neural activity.

372 **Code availability**

373 We have published an open-source toolbox implementing the SuperEEG algorithm. It may be
374 downloaded [here](#).

375 **Data availability**

376 The dataset analyzed in this study was generously shared by Michael Kahana. A portion of
377 Dataset 1 may be downloaded [here](#). Dataset 2 may be downloaded [here](#).

378 **Acknowledgements**

379 We are grateful for useful discussions with Luke J. Chang, Uri Hasson, Josh Jacobs, Michael
380 Kahana, and Matthijs van der Meer. We are also grateful to Michael Kahana for generously
381 sharing the ECoG data we analyzed in our paper, which was collected under NIMH grant
382 MH55687 and DARPA RAM Cooperative Agreement N66001-14-2-4-032, both to MJK. Our
383 work was also supported in part by NSF EPSCoR Award Number 1632738 and by a sub-
384 award of DARPA RAM Cooperative Agreement N66001-14-2-4-032 to JRM. The content is solely
385 the responsibility of the authors and does not necessarily represent the official views of our
386 supporting organizations.

³⁸⁷ **Author Contributions**

³⁸⁸ J.R.M conceived and initiated the project. L.L.W.O. and A.C.H. performed the analyses. J.R.M.
³⁸⁹ and L.L.W.O. wrote the manuscript.

³⁹⁰ **Author Information**

³⁹¹ Reprints and permissions information is available at www.nature.com/reprints. The authors
³⁹² declare no competing financial interests. Readers are welcome to comment on the online
³⁹³ version of the paper. Publisher's note: Springer Nature remains neutral with regard to jurisdic-
³⁹⁴ tional claims in published maps and institutional affiliations. Correspondence and requests for
³⁹⁵ materials should be addressed to J.R.M. (jeremy.r.manning@dartmouth.edu).

³⁹⁶ **References**

- ³⁹⁷ [1] Baillet, S., Mosher, J. C., and Leahy, R. M. (2001). Electromagnetic brain mapping. *IEEE
398 Signal Processing Magazine*, 18:14–30.
- ³⁹⁹ [2] Becker, C. O., Pequito, S., Pappas, G. J., Miller, M. B., adn D S Bassett, S. T. G., and Preciado,
400 V. M. (2018). Spectral mapping of brain functional connectivity from diffusion imaging.
401 *Scientific Reports*, 8(1411):<https://doi.org/10.1038/s41598-017-18769-x>.
- ⁴⁰² [3] Betzel, R. F., Medaglia, J. D., Kahn, A. E., Soffer, J., Schonhaut, D. R., and Bassett, D. S.
403 (2017). Inter-regional ecog correlations predicted by communication dynamics, geometry,
404 and correlated gene expression. *arXiv*, page 1706.06088.
- ⁴⁰⁵ [4] Casey, B. J., Giedd, J. N., and Thomas, K. M. (2000). Structural and functional brain devel-
406 opment and its relation to cognitive development. *Biological Psychology*, 54(1–3):241–257.
- ⁴⁰⁷ [5] Cole, M. W., Ito, T., Bassett, D. S., and Schultz, D. H. (2016). Activity flow over resting-state
408 networks shapes cognitive task activations. *Nature Neuroscience*, 19(12):1718–1726.

- 409 [6] Crone, N. E., Korzeniewska, A., and Franaszczuk, P. (2011). Cortical gamma responses:
410 searching high and low. *International Journal of Psychophysiology*, 79(1):9–15.
- 411 [7] Ezzyat, Y., Kragel, J. E., Burke, J. F., Levy, D. F., Lyalenko, A., Wanda, P., O’Sullivan, L.,
412 Hurley, K. B., Busygin, S., Pedisich, I., Sperling, M. R., Worrell, G. A., Kucewicz, M. T., Davis,
413 K. A., Lucas, T. H., Inman, C. S., Lega, B. C., Jobst, B. C., Sheth, S. A., Zaghloul, K., Jutras,
414 M. J., Stein, J. M., Das, S. R., Gorniak, R., Rizzuto, D. S., and Kahana, M. J. (2017). Direct
415 brain stimulation modulates encoding states and memory performance in humans. *Current
Biology*, 27:1–8.
- 416
- 417 [8] Ezzyat, Y., Wanda, P. A., Levy, D. F., Kadel, A., Aka, A., Pedisich, I., Sperling, M. R.,
418 Sharan, A. D., Lega, B. C., Burks, A., Gross, R. E., Inman, C. S., Jobst, B. C., Goren-
419 stein, M. A., Davis, K. A., Worrell, G. A., Kucewicz, M. T., Stein, J. M., Gorniak, R.,
420 Das, S. R., Rizzuto, D. S., and Kahana, M. J. (2018). Closed-loop stimulation of tem-
421 poral cortex rescues functional networks and improves memory. *Nature Communications*,
422 9(365):<https://doi.org/10.1038/s41467-017-02753-0>.
- 423
- 424 [9] Finn, E. S., Shen, X., Scheinost, D., Rosenberg, M. D., Huang, J., Chun, M. M., Papademetris,
425 X., and Constable, R. T. (2015). Functional connectome fingerprinting: identifying individuals
using patterns of brain connectivity. *Nature Neuroscience*, 18:1664 – 1671.
- 426
- 427 [10] Grabner, G., Janke, A. L., Budge, M. M., Smith, D., Pruessner, J., and Collins, D. L. (2006).
428 Symmetric atlasing and model based segmentation: an application to the hippocampus in
older adults. *Medical Image Computing and Computer-Assistend Intervention*, 9:58–66.
- 429
- 430 [11] Hillebrand, A., Singh, K. D., Holliday, I. E., Furlong, P. L., and Barnes, G. R. (2005). A new
431 approach to neuroimaging with magnetoencephalography. *Human Brain Mapping*, 25:199–
211.

- 432 [12] Horak, P. C., Meisenhelter, S., Song, Y., Testorf, M. E., Kahana, M. J., Viles, W. D., Bujarski,
433 K. A., Connolly, A. C., Robbins, A. A., Sperling, M. R., Sharan, A. D., Worrell, G. A., Miller,
434 L. R., Gross, R. E., Davis, K. A., Roberts, D. W., Lega, B., Sheth, S. A., Zaghloul, K. A., Stein,
435 J. M., Das, S. R., Rizzuto, D. S., and Jobst, B. C. (2017). Interictal epileptiform discharges
436 impair word recall in multiple brain areas. *Epilepsia*, 58(3):373–380.
- 437 [13] Huster, R. J., Debener, S., Eichele, T., and Herrmann, C. S. (2012). Methods for simultaneous
438 EEG-fMRI: an introductory review. *The Journal of Neuroscience*, 32(18):6053–6060.
- 439 [14] Jacobs, J., Kahana, M. J., Ekstrom, A. D., Mollison, M. V., and Fried, I. (2010). A sense of
440 direction in human entorhinal cortex. *Proceedings of the National Academy of Sciences, USA*,
441 107(14):6487–6482.
- 442 [15] Jahanshad, N., Kochunov, P. V., Sprooten, E., Mandl, R. C., Nichols, T. E., Almasy, L.,
443 Blangero, J., Brouwer, R. M., Curran, J. E., de Zubicaray, G. I., Duggirala, R., Fox, P. T., Hong,
444 L. E., Landman, B. A., Martin, N. G., McMahon, K. L., Medland, S. E., Mitchell, B. D., Olvera,
445 R. L., Peterson, C. P., Starr, J. M., Sussmann, J. E., Toga, A. W., Wardlaw, J. M., Wright, M. J.,
446 Pol, H. E. H., Pastin, M. E., McIntosh, A. M., Deary, I. J., Thompson, P. M., and Glahn, D. C.
447 (2013). Multi-site genetic analysis of diffusion images and voxelwise heritability analysis: A
448 pilot project of the enigma-dti working group. *NeuroImage*, 81(1):455–469.
- 449 [16] Kragel, J. E., Ezzyat, Y., Sperling, M. R., Gorniak, R., Worrell, G. A., Berry, B. M., Inman,
450 C., Lin, J.-J., Davis, K. A., Das, S. R., Stein, J. M., Jobst, B. C., Zaghloul, K. A., Sheth, S. A.,
451 Rizzuto, D. S., and Kahana, M. J. (2017). Similar patterns of neural activity predict memory
452 formation during encoding and retrieval. *NeuroImage*, 155:70–71.
- 453 [17] Kucewicz, M. T., Berry, B. M., Kremen, V., Brinkmann, B. H., Sperling, M. R., Jobst, B. C.,
454 Gross, R. E., Lega, B., Sheth, S. A., Stein, J. M., Das, S. R., Gorniak, R., Stead, S. M., Rizzuto,

- 455 D. S., Kahana, M. J., and Worrell, G. A. (2017). Dissecting gamma frequency actiivty during
456 human memory processing. *Brain*, 140:1337–1350.
- 457 [18] Kucewicz, M. T., Berry, B. M., Miller, L. R., Khadjevand, F., Ezzyat, Y., Stein, J. M., Kremen,
458 V., Brinkmann, B. H., Wanda, P., Sperling, M. R., Gorniak, R., Davis, K. A., Jobst, B. C., Gross,
459 R. E., Lega, B., Gompel, J. V., Stead, S. M., Rizzuto, D. S., Kahana, M. J., and Worrell, G. A.
460 (2018). Evidence for verbal memory enhancement with electrical brain stimulation in the
461 lateral temporal cortex. *Brain*, 141(4):971–978.
- 462 [19] Lin, J.-J., Rugg, M. D., Das, S., Stein, J., Rizzuto, D. S., Kahana, M. J., and Lega, B. C.
463 (2017). Theta band power increases in the posterior hippocampus predict successful episodic
464 memory encoding in humans. *Hippocampus*, 27:1040–1053.
- 465 [20] Manning, J. R., Jacobs, J., Fried, I., and Kahana, M. J. (2009). Broadband shifts in LFP power
466 spectra are correlated with single-neuron spiking in humans. *The Journal of Neuroscience*,
467 29(43):13613–13620.
- 468 [21] Manning, J. R., Polyn, S. M., Baltuch, G., Litt, B., and Kahana, M. J. (2011). Oscillatory
469 patterns in temporal lobe reveal context reinstatement during memory search. *Proceedings of
470 the National Academy of Sciences, USA*, 108(31):12893–12897.
- 471 [22] Manning, J. R., Ranganath, R., Norman, K. A., and Blei, D. M. (2014). Topographic
472 factor analysis: a Bayesian model for inferring brain networks from neural data. *PLoS One*,
473 9(5):e94914.
- 474 [23] Manning, J. R., Sperling, M. R., Sharan, A., Rosenberg, E. A., and Kahana, M. J. (2012).
475 Spontaneously reactivated patterns in frontal and temporal lobe predict semantic clustering
476 during memory search. *The Journal of Neuroscience*, 32(26):8871–8878.

- 477 [24] Manning, J. R., Zhu, X., Willke, T. L., Ranganath, R., Stachenfeld, K., Hasson, U., Blei,
478 D. M., and Norman, K. A. (2018). A probabilistic approach to discovering dynamic full-brain
479 functional connectivity patterns. *NeuroImage*.
- 480 [25] Miller, K. J., Shenoy, P., den Nijs, M., Sorensen, L. B., Rao, R. P. N., and Ojemann, J. G. (2008).
481 Beyond the gamma band: the role of high-frequency features in movement classification.
482 *IEEE Transactions on Biomedical Engineering*, 55(5):1634 – 1637.
- 483 [26] Mori, S., Oishi, K., Jiang, H., Jiang, L., Li, X., Akhter, K., Hua, K., Faria, A. V., Mahmood,
484 A., Woods, R., Toga, A. W., Pike, G. B., Neto, P. R., Evans, A., Zhang, J., Huang, H., Miller,
485 M. I., van Zijl, P., and Mazziotta, J. (2008). Stereotaxic white matter atlas based on diffusion
486 tensor imaging in an icbm template. *NeuroImage*, 40(2):570–582.
- 487 [27] Rasmussen, C. E. (2006). *Gaussian processes for machine learning*. MIT Press.
- 488 [28] Sarvas, J. (1987). Basic mathematical and electromagnetic concepts of the biomagnetic
489 inverse problem. *Phys. Med. Biol.*, 32(1):11–22.
- 490 [29] Sawyer, R. J. (1995). *The Terminal Experiment*. HarperPrism.
- 491 [30] Sederberg, P. B., Kahana, M. J., Howard, M. W., Donner, E. J., and Madsen, J. R. (2003). Theta
492 and gamma oscillations during encoding predict subsequent recall. *Journal of Neuroscience*,
493 23(34):10809–10814.
- 494 [31] Sederberg, P. B., Schulze-Bonhage, A., Madsen, J. R., Bromfield, E. B., Litt, B., Brandt,
495 A., and Kahana, M. J. (2007a). Gamma oscillations distinguish true from false memories.
496 *Psychological Science*, 18(11):927–932.
- 497 [32] Sederberg, P. B., Schulze-Bonhage, A., Madsen, J. R., Bromfield, E. B., McCarthy, D. C.,
498 Brandt, A., Tully, M. S., and Kahana, M. J. (2007b). Hippocampal and neocortical gamma
499 oscillations predict memory formation in humans. *Cerebral Cortex*, 17(5):1190–1196.

- 500 [33] Sejnowski, T. J., Churchland, P. S., and Movshon, J. A. (2014). Putting big data to good use
501 in neuroscience. *Nature Neuroscience*, 17:1440–1441.
- 502 [34] Snyder, A. Z. (1991). Dipole source localization in the study of EP generators: a critique.
503 *Electroencephalography and Clinical Neurophysiology*, 80(4):321–325.
- 504 [35] Solomon, E. A., Gross, R., Lega, B., Sperling, M. R., Worrell, G., Sheth, S. A., Zaghloul,
505 K. A., Jobst, B. C., Stein, J. M., Das, S., Gorniak, R., Inman, C., Seger, S., Kragel, J. E., Rizzuto,
506 D. S., and Kahana, M. J. (2018). Mtl functional connectivity predicts stimulation-induced
507 theta power. *Nature Communications*, In press.
- 508 [36] Sporns, O. and Betzel, R. F. (2016). Modular brain networks. *Annual Review of Psychology*,
509 67:613–640.
- 510 [37] Talairach, J. and Tournoux, P. (1988). *Co-planar stereotaxic atlas of the human brain*. Verlag,
511 Stuttgart.
- 512 [38] Tavor, I., Jones, O. P., Mars, R. B., Smith, S. M., Behrens, T. E., and Jbabdi, S. (2016). Task-
513 free MRI predicts individual differences in brain activity during task performance. *Science*,
514 352(6282):216–220.
- 515 [39] Turk-Browne, N. B. (2013). Functional interactions as big data in the human brain. *Science*,
516 342:580–584.
- 517 [40] Weidemann, C. T., Kragel, J. E., Lega, B. C., Worrell, G. A., Sperling, M. R., Sharan, A. D.,
518 Jobst, B. C., Khadjevand, F., Davis, K. A., Wanda, P. A., Kadel, A., Rizzuto, D. S., and Kahana,
519 M. J. (2018). Neural activity reveals interactions between episodic and semantic memory
520 systems during retrieval. *Journal of Experimental Psychology: General*, In press.
- 521 [41] Yeo, B. T. T., Krienen, F. M., Sepulcre, J., Sabuncu, M. R., Lashkari, D., Hollinshead, M.,
522 Roffman, J. L., Smoller, J. W., Zollei, L., Polimieni, J. R., Fischl, B., Liu, H., and Buckner,

- 523 R. L. (2011). The organization of the human cerebral cortex estimated by intrinsic functional
- 524 connectivity. *Journal of Neurophysiology*, 106(3):1125–1165.